Importance of electron-impurity scattering for electron transport in terahertz quantum-cascade lasers

Hans Callebaut, Sushil Kumar, Benjamin S. Williams, and Qing Hu[a)]
Department of Electrical Engineering and Computer Science and Research Laboratory of Electronics, Massachusetts Institute of Technology, Cambridge, Massachusetts 02139

John L. Reno
Sandia National Laboratories, Department 1123, MS 0601, Albuquerque, New Mexico 87185-0601

(Received 21 October 2003; accepted 29 November 2003)

Using an ensemble Monte Carlo simulation, including both electron–electron and electron–phonon scattering as well as electron-impurity scattering, the current density, population inversion, electron temperature, and gain in two THz quantum-cascade structures are investigated and compared to measurements. We find that the inclusion of electron-impurity scattering in the calculations is crucial when modeling the intersubband transport dynamics in these devices. However, the calculated gain is higher than inferred from experiments. This can be attributed to wavefunction localization caused by dephasing scattering, which is unaccounted for in the present model. © *2004 American Institute of Physics.* [DOI: 10.1063/1.1644337]

Recently, the operating frequency range of quantum-cascade lasers (QCLs) has been extended from the mid-infrared to the far-infrared below the Reststrahlen band [terahertz (THz) frequencies].[1–3] Especially for THz QCLs, a detailed understanding of the dynamics of electron transport is essential in order to extend their operation to longer wavelengths and higher temperatures. Compared to mid-infrared structures, the subband separations in THz QCLs are much smaller, which greatly influences electron transport. In particular, since the radiative transition energy $\hbar\omega$ is smaller than the LO-phonon energy $\hbar\omega_{\mathrm{LO}}$, the nonradiative relaxation rate is highly temperature dependent due to thermally activated LO-phonon scattering. The reduced subband separation also increases the importance of scattering processes which favor small transition energies, such as electron–electron (e–e), electron-impurity (e–imp), and interface roughness scattering. Therefore, in a proper analysis of electron transport in a THz QCL, all the aforementioned elastic and inelastic scattering mechanisms should be accounted for. Indeed, earlier work has clearly indicated that electron–phonon (e–ph) and e–e scattering alone are insufficient to explain the measured current densities.[4]

Lee and Wacker[5] presented a comprehensive model for electron transport, based on nonequilibrium Green's functions. However, most QCL analyses and calculations[4,6–8] have only considered e–ph and e–e scattering. Although the effects of impurity[9] and interface roughness scattering[10] on the spontaneous emission linewidth are well documented and generally accepted, their importance for electron transport in QCLs has been largely ignored. The study of e–imp scattering in the electron transport dynamics has been mostly restricted to the relaxation of excited carriers in quantum wells.[11,12]

It should be pointed out that ionized impurities and interface imperfections are static scatterers, and therefore it is always possible to rediagonalize the Hamiltonian to get stationary wavefunctions that take into account the modified potential landscape. In such a picture, the imperfections would not cause any intereigenstate scattering per se. The in-plane translational symmetry would be destroyed, and transitions would take place between manifolds of states with in-plane position dependence, resulting in linewidth broadening. However, in simulations a perturbative approach (treating impurities and imperfections as random scatterers in an otherwise perfect lattice) is preferable. This approach allows us to describe the in-plane component of the wavefunction as a plane wave, which vastly reduces the calculation's complexity and preserves an intuitive picture of intersubband transitions.

Interface roughness scattering rates depend sensitively on the details and conditions of the growth, and will vary widely with samples. This makes interface roughness scattering impossible to quantify in a universal way without introducing phenomenological parameters. In contrast, the distribution of ionized impurities in a sample can be modeled accurately. Due to these considerations, we have chosen to focus on e–imp scattering. As will be shown, its importance in intersubband transport rivals or even exceeds that of e–e scattering, and this cannot be neglected.

Both e–imp and e–e scattering are Coulombic interactions, which allows for a simple assessment of their relative importance. Assuming charge neutrality, the number of electrons and ions are the same and, hence, the number of possible scattering centers is equal for both processes. However, due to the exchange interaction, e–e scattering is mostly caused by interactions between electrons of opposite spins.[13] Also, in a center-of-mass frame, e–e scattering can be described with a reduced mass $m_r^*=m^*/2$, whereas for e–imp scattering $m_r^*=m^*$. Furthermore, intersubband e–e scattering largely originates from interactions between electrons in the same subband. Impurity scattering, on the other hand, is limited by its dependence on the distance $|z-z_{\mathrm{imp}}|$ between the scattering electron and the ionized impurity, and as such

a)Electronic mail: qhu@mit.edu

is most effective for transport between subbands whose wavefunctions $\chi(z)$ are close to the doping layer. This rough estimate of the relative importance of e–e and e–imp scattering[12] can be summarized as

$$\frac{W_{if}^{\mathrm{e-e}}}{W_{if}^{\mathrm{imp}}} \propto \frac{1}{4}\frac{N_i|F_{iiff}^{\mathrm{e-e}}(q)|^2}{N_{\mathrm{imp}}|F_{if}^{\mathrm{imp}}(q)|^2}. \tag{1}$$

Here $W_{if}^{\mathrm{e-e}}$ and W_{if}^{imp} are, respectively, the e–e and e–imp scattering rates from $n=i$ into $n=f$, N_i is the population density in subband i, N_{imp} is the total doping density, and the form factors[12] F are functions of the exchanged momentum q. The factor-of-four reduction arises from the exchange interaction and reduced mass discussed earlier. Clearly, for intersubband transport, e–imp scattering usually dominates over e–e scattering and adds significantly to electron gas heating. However, e–imp scattering does not allow for energy exchange between electrons, and therefore does not contribute to intrasubband carrier thermalization as e–e scattering does.

To illustrate the importance of impurity scattering in electron transport in THz QCLs, Monte Carlo (MC) simulations[4] were used to investigate several different QC designs. In this letter we focus on two representative examples, for which experimental results were published. All simulations include e–ph (acoustic and LO-phonon) and e–e scattering. Calculations were performed with and without e–imp scattering. A nonequilibrium, multisubband screening model[14] was implemented for e–imp and e–e interactions. No phenomenological parameters were introduced. When comparing the calculation results with the measurements, the current density J provides a good reference point. Only when the simulation produces current densities consistent with experiments can we have confidence in other calculated results, such as subband populations and gain. Note that, in this letter, all scattering times are net scattering rates and include the effect of backfilling.[4]

The first investigated device is the 3.4-THz QCL[3] [Fig. 1(a)] that was previously discussed in Ref. 4 using a MC simulation without e–imp scattering. Table I and Fig. 2 show a comparison of the key MC results with and without e–imp scattering, for a lattice temperature $T_{\mathrm{latt}}=25$ K. Note that the inclusion of e–imp scattering results in an increase in electron temperature. Also, the calculated J at injection anticrossing (~ 65 mV/module) increases from 580 to 950 A/cm^{-2}. The simulation result closely tracks the measured current density for biases larger than 55 mV/module, in the range where no large parasitic current channels[4] are present. The increase in J is due to an enhanced scattering rate in the injector region (between $n=2'$ and $n=1'$), and between $n=1'$ and the upper radiative state $n=5$. τ_{21} decreases from 14 to 5 ps due to $\tau_{21}^{\mathrm{imp}}=7$ ps, eliminating the population inversion between $n=2'$ and $n=1'$, in contrast to the result in Ref. 15. In spite of the decrease in $\tau_{1'5}=4.5$ ps (from 6 ps without e–imp scattering), the population density of $n=5$ remains almost unchanged because of the increased thermally activated LO-phonon scattering ($\tau_5^{\mathrm{LO}}\approx 2.8$ ps from 4.1 ps). Note that, although e–imp scattering between the radiative levels ($\tau_{54}^{\mathrm{imp}}=23$ ps) is faster than e–e scattering ($\tau_{54}^{\mathrm{e-e}}=49$ ps), its (direct) contribution to the depopulation of $n=5$ is negligible. τ_4 is dominated by resonant LO-phonon scattering, and is little affected by e–imp scattering. However, the rise in J results in a slight population increase in $n=4$. Using measured values[16] for the refractive index $n=3.8$ and the linewidth $\Delta\nu=1$ THz, and the calculated population inversion $\Delta N_{54}=5.8\times 10^{10}$ cm^{-2}, a peak gain of 73 cm^{-1} is found (68 cm^{-1} without e–imp scattering). This value slightly exceeds the upper limit of the gain range inferred from experiments, which is most likely due to the neglect of wavefunction localization caused by incoherent transport through the injector barrier (anticrossing $\Delta_{1'5}\approx 1.8$ MeV).

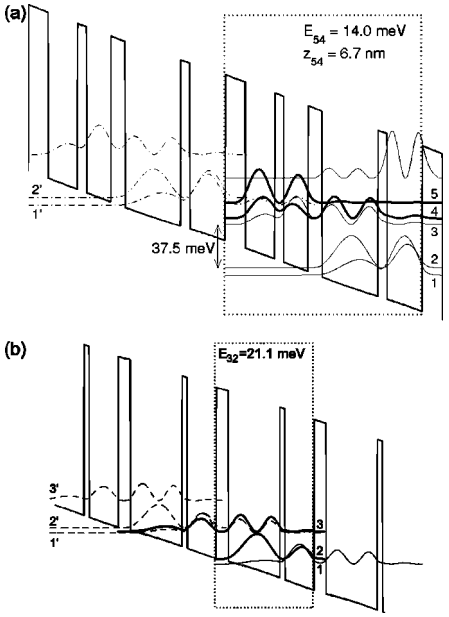

FIG. 1. (a) Band structure for the 3.4-THz laser. The device consists of GaAs/$Al_{0.15}Ga_{0.85}$As layers with thicknesses (nm) **5.4**/7.8/**2.4**/6.4/**3.8**/14.8/**2.4**/9.4 (barriers in boldface, wells in plain text) and is doped to $n=1.9\times 10^{16}$ cm^{-3} in the 14.8 nm wide well, resulting in a sheet density of 2.8×10^{10} cm^{-2} per module. (b) Band structure for the two-well structure. The device consists of GaAs/$Al_{0.15}Ga_{0.85}$As layers with thicknesses (nm) **5.5**/23.4/**2.4**/13.2 and a doping concentration $n=1.4\times 10^{16}$ cm^{-3} in the 13.2 nm wide well, resulting in a sheet density of 1.85×10^{10} cm^{-2} per module.

The second QC device is a simple double-quantum-well structure,[17] which is shown in Fig. 1(b). In experiments, the current characteristics of this device were nearly independent of temperature for $T_{\mathrm{latt}}=5-77$ K, while the electroluminescence dropped sharply. This is a strong indication that transport through the thick injector barrier is limited by incoherent tunneling between the injector state and the upper radiative level (anticrossing $\Delta_{1'3}\approx 0.8$ MeV). In such a case, the use of extended wavefunctions for transport analysis would be expected to overestimate J. Table II and Fig. 3

TABLE I. Calculated subband energy, temperature, and population density of the 3.4 THz laser at injection anticrossing ($T_{\mathrm{latt}}=25$ K) with and without impurity scattering.

		T_{el} (K)		Pop. (10^{10} cm^{-2})	
n	E (meV)	Without imp.	With imp.	Without imp.	With imp.
1	0	102	121	0.77	0.98
2	6.5	111	139	1.29	0.95
3	44.0	122	145	0.10	0.12
4	49.3	133	160	0.08	0.12
5	63.3	96	117	0.64	0.70

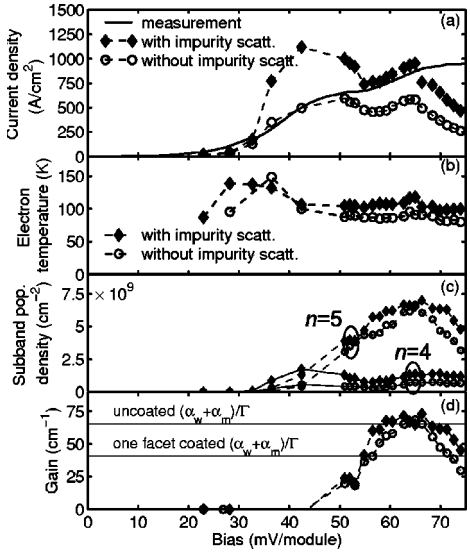

FIG. 2. Key results of the MC simulation of the 3.4-THz laser for $T_{\text{latt}} = 25$ K, calculated with and without e–imp scattering (represented by diamonds and circles, respectively). (a) J for a range of biases. The measured current density (solid line) was adjusted to account for a parasitic series resistance of 2 Ω. The large parasitic current peak of ~ 2000 A/cm^2 at ~ 45 mV/module was omitted from the calculation results. (b) T_{el} for $n = 5$, the upper radiative level. (c) The population density in $n = 4$ (solid line) and $n = 5$ (dashed line). (d) Material gain for a 1180×150 μm^2 ridge structure. The two horizontal lines represent the total cavity losses with uncoated facets and with one facet fully reflecting.

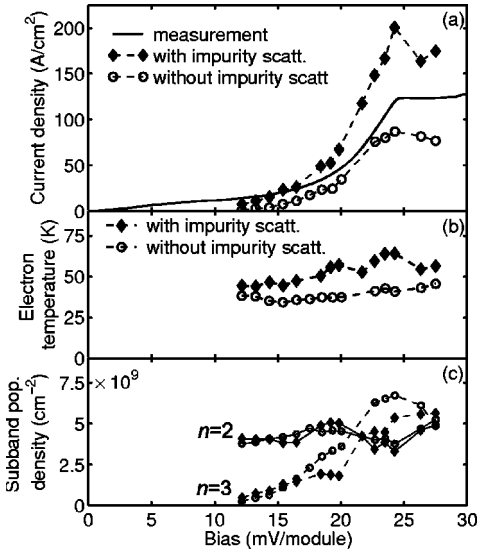

FIG. 3. Key results of the MC simulation of the two-well structure for $T_{\text{latt}} = 25$ K, calculated with and without e–imp scattering (represented by diamonds and circles, respectively). (a) J for a range of biases. The measured current density (solid line) was adjusted to take into account a parasitic series resistance of 1.5 Ω. (b) T_{el} for $n = 3$, the upper radiative level. (c) The population density in $n = 2$ (solid line) and $n = 3$ (dashed line).

present the main calculation results with and without e–imp scattering, for $T_{\text{latt}} = 25$ K. Figure 3(a) shows that the inclusion of e–imp scattering is necessary to obtain the expected overestimation of the peak current density. As with the 3.4-THz laser, the increase in current can be explained by the enhancement of transport through the collector state due to e–imp scattering, combined with a decline in τ_3 caused largely by thermally activated LO-phonon scattering ($\tau_3^{\text{LO}} \approx 13$ ps, compared to 35 ps without e–imp scattering). The calculated lifetime of $n = 2$ is reduced from $\tau_2 \approx \tau_2^{\text{e–e}} = 13$ ps to 4 ps by the inclusion of $\tau_2^{\text{imp}} = 6$ ps. The poor agreement between calculation and experiment for this device is likely due to the small anticrossing gap $\Delta_{1'3} \approx 0.8$ meV.

In conclusion, we have demonstrated the importance of impurity scattering in the dynamics of intersubband transport in THz QCLs and compared the calculated $I-V$ characteristics with experimental measurements. The inclusion of e–imp scattering in MC simulations eliminates a serious problem from the previous work, i.e., underestimation of the current density. All simulation results including e–imp scattering, both of the devices discussed in this letter and of other designs, have consistently yielded an overestimated J. In our current model, using spatially extended wavefunctions without including the effect of dephasing, the calculated current density should always exceed the experimental values, which result from a combination of sequential tunneling and intersubband scattering.

TABLE II. Calculated subband energy, temperature, and population density of the two-well device at injection anticrossing ($T_{\text{latt}} = 25$ K) with and without impurity scattering.

		T_{el} (K)		Pop. (10^{10} cm^{-2})	
n	E (meV)	Without imp.	With imp.	Without imp.	With imp.
1	0	42	50	0.80	0.99
2	3.9	54	85	0.38	0.33
3	25.0	43	64	0.67	0.53

The authors would like to thank S. Goodnick for generously allowing them to adapt his MC code. This work is supported by AFOSR, NASA, and NSF. Sandia is a multiprogram laboratory operated by Sandia Corporation, a Lockheed Martin company, for the United States Department of Energy under Contract No. DE-AC04-94AL85000.

[1] R. Köhler, A. Tredicucci, F. Beltram, H. E. Beere, E. H. Linfield, A. G. Davis, D. A. Ritchie, R. C. Iotti, and F. Rossi, Nature (London) **417**, 156 (2002).
[2] M. Rochat, L. Ajili, H. Willenberg, J. Faist, H. Beere, G. Davis, E. Linfield, and D. Ritchie, Appl. Phys. Lett. **81**, 1381 (2002).
[3] B. S. Williams, H. Callebaut, S. Kumar, Q. Hu, and J. L. Reno, Appl. Phys. Lett. **82**, 1015 (2003).
[4] H. Callebaut, S. Kumar, B. S. Williams, Q. Hu, and J. L. Reno, Appl. Phys. Lett. **83**, 207 (2003).
[5] S. C. Lee and A. Wacker, Phys. Rev. B **66**, 245314 (2002).
[6] R. Köhler, R. C. Iotti, A. Tredicucci, and F. Rossi, Appl. Phys. Lett. **79**, 3920 (2001).
[7] F. Compagnone, A. Di Carlo, and P. Lugli, Appl. Phys. Lett. **80**, 920 (2002).
[8] D. Indjin, P. Harrison, R. W. Kelsall, and Z. Ikonić, Appl. Phys. Lett. **82**, 1347 (2003).
[9] J. Faist, F. Capasso, C. Sirtori, D. L. Sivco, A. L. Hutchinson, S. N. G. Chu, and A. Y. Cho, Appl. Phys. Lett. **65**, 94 (1994).
[10] H. Sakaki, T. Noda, K. Hirakawa, M. Tanaka, and T. Matsusue, Appl. Phys. Lett. **51**, 1934 (1987).
[11] S. M. Goodnick and P. Lugli, Appl. Phys. Lett. **51**, 584 (1987).
[12] M. Dür, S. M. Goodnick, and P. Lugli, Phys. Rev. B **54**, 17794 (1996).
[13] C. J. Hearn, *The Physics of Nonlinear Transport in Semiconductors*, edited by D. K. Ferry, J. R. Barker, and C. Jacoboni (Plenum, New York, 1980).
[14] T. Ando, A. B. Fowler, and F. Stern, Rev. Mod. Phys. **54**, 437 (1982).
[15] S. C. Lee and A. Wacker, Appl. Phys. Lett. **83**, 2506 (2003).
[16] B. S. Williams, S. Kumar, H. Callebaut, Q. Hu, and J. L. Reno, Electron. Lett. **39**, 915 (2003).
[17] B. S. Williams, H. Callebaut, Q. Hu, and J. L. Reno, Appl. Phys. Lett. **79**, 4444 (2001).